ORNL/TM-2023/3009

Towards Realistic and High Fidelity Models for Nuclear Reactor Power Synthesis Simulation with Self-Powered Neutron Detectors

Anthony Birri
K. C. Goetz
Daniel C. Sweeney
N. Dianne Bull Ezell

August 2023

OAK RIDGE National Laboratory

ORNL IS MANAGED BY UT-BATTELLE LLC FOR THE US DEPARTMENT OF ENERGY

ORNL/TM-2023/3009

Nuclear Energy and Fuel Cycle Division

Towards Realistic and High Fidelity Models for Nuclear Reactor Power Synthesis Simulation with Self-Powered Neutron Detectors

Anthony Birri, K. C. Goetz, Daniel C. Sweeney, N. Dianne Bull Ezell

August 2023

Prepared by
OAK RIDGE NATIONAL LABORATORY
Oak Ridge, TN 37831
managed by
UT-Battelle LLC
for the
US DEPARTMENT OF ENERGY
under contract DE-AC05-00OR22725

CONTENTS

ABBREVIATIONS

BEACON	Best Estimate Analyzer for Core Operation - Nuclear
BOL	beginning of life
BWR	boiling water reactor
CE	Combustion Engineering
CSC	cubic spline synthesis
GE	General Electric
Geant	Geometry and Tracking
GMDH	group method of data handling
IPD	Infer Power Distribution [script]
PBI	point-based iterative
MCNP	Monte Carlo N-Particle
PD	Power Distributions [script]
PWR	pressurized water reactor
RFP	Response Function Parameters [script]
RG	Reactor Geometries [script]
SMR	small modular reactor
SPND	self power neutron detector
SSR	surface source read
SSW	surface source write
TAMU TRIGA	Texas A&M Testing, Research, Isotopes, General Atomics Reactor

ACKNOWLEDGEMENTS

This work is funded by the US Department of Energy's Advanced Sensors and Instrumentation Program. The authors would like to acknowledge Tyler Gates for developing the MCNP model of the TAMU TRIGA reactor, which is used for the study herein, in his graduate studies at Texas A&M University.

SUMMARY

As presented in this report, a weighting function–based inferencing method is being applied to synthesize the power distribution in next-generation and university research reactors based on simulated self power neutron detector (SPND) responses. The overall goal is to assess the impacts of sensor uncertainty and true power distribution perturbations on the error in the synthesized power distribution. Regarding sensor uncertainty, the NuScale Small Modular Reactor (SMR) and the Westinghouse AP1000 serve as testbeds for analyzing the impact of varying the sensor uncertainty, as well as varying the number of sensors per sensor string in the reactor core. The reactor models are informed by Monte Carlo N-Particle (MCNP) neutron flux tallies. For the NuScale SMR and Westinghouse AP1000, the SPND response functions (i.e., the response of the SPNDs to individual segments of fuel) were determined homogeneously. Regarding an analysis of power distribution perturbation detection, the Texas A&M Testing, Research, Isotopes, General Atomics Reactor (TAMU TRIGA) reactor was used as a demonstration case with one particular arrangement of SPNDs; the response functions for this reactor model were determined heterogeneously, making this a uniquely high-fidelity demonstration of perturbation detection. Finally, SPND models generated in the Geometry and Tracking 4 (Geant4) code have been generated and tested for comparison with traditionally implemented analytical SPND models, with the intent for Geant4 integration with the full methodological framework. SPND current outputs as a function of distance from some fuel assembly segment in the NuScale SMR are compared with the analytically determined currents.

Results from the sensor uncertainty simulations for the NuScale SMR and AP1000 indicate that the average error in the inferred power distribution on the fuel assembly segment level is reasonably low, being slightly less than the random uncertainty applied to all respective SPNDs in both cores. For example, if all SPNDs in the core have a random uncertainty of 5%, then the corresponding fuel assembly segment level error (i.e. difference between the true and inferred local power) is ~2–3%. However, the maximum error in the inferred power distribution on the fuel assembly segment level can be considerably high (>15%) when SPND random uncertainties start to exceed ~3%. In general, the average and maximum errors in the inferred power distribution were slightly higher in the AP1000 as opposed to the NuScale SMR for the sensor string configurations considered herein. Another result determined from analysis of the sensor uncertainty simulations was that increasing the number of SPNDs per string does not clearly reduce inferred power distribution error and can in fact make the error large in some cases; however, this assessment may skewed due to imposed iteration limits. Results from the perturbation detection demonstration using the high-fidelity TAMU TRIGA model indicate that, given the arrangement of 17 SPND strings and 4 SPNDs per string considered herein, there is a clear, provable ability to infer a localized Gaussian-type peak perturbation in the 3D power distribution. Such a perturbation was detected with an average fuel assembly segment level error of 0.19%, and the general visualization of the detected perturbation clearly indicates that the magnitude and shape were appropriately resolved. Finally, the electrical current output generated by the Geant4 modeled SPND indicates significant magnitude differences than the analytically modeled SPND, demonstrating the need for accurate SPND models which account for finite sensor geometry effects to inform the power synthesis work described herein.

1 BACKGROUND

To ensure the safe, efficient, effective operation of nuclear power plants, it is crucial that the reactor core power distribution is actively inferred throughout the operational timeline. Over the life of the core, the power distribution will be subject to perturbations relating to fuel burnup or burnable absorber material,

variations in coolant temperature, pressure, or flow conditions, build-in of Xe-135, and movement of control rods [1, 2, 3, 4, 5, 6, 7]. In general, power distribution inferencing (also called *power shape synthesis*) is achieved by collecting data from an array of in-core or ex-core sensors and using this data to inform reconstruction methods to determine power distribution. Frequently updated core power distribution of sufficient fidelity can inform reactor operators or autonomous control systems to control spatial power perturbations through strategic control rod movements. In addition, online power distribution monitoring can enable improved diagnostics in accident scenarios, because power distribution characteristics up to and during an accident event may provide useful information about the root cause.

Power inferencing methods have been actively implemented for the past few decades in the current US reactor fleet. Westinghouse uses the Best Estimate Analyzer for Core Operation - Nuclear (Beacon) for core monitoring in pressurized water reactors (PWRs). Beacon was first publicized in 1994, and several updates were made in the 2000s and 2010s to incorporate different types of detectors, integral thermal hydraulics, and uncertainty evaluation [8, 9, 10, 11, 12]. General Electric (GE) also has a core monitoring system called ACUMEN (formerly 3D-MONICORE) which can generate the nodal power distribution and associated uncertainties in GE boiling water reactors (BWRs) [13, 14]. Combustion Engineering (CE) developed an in-core detector analysis system in the 1980s called CECOR to determine radial and axial power distributions in PWRs based on self-powered neutron detector (SPND) responses; operational experience has been disseminated based on application in Arkansas Nuclear One Unit 2 [15]. Because of the proprietary nature of these software packages, details regarding mathematical formalism, data processing algorithms, and uncertainty analysis are severely limited in public documentation. It is likely that either Westinghouse or GE is either fully or partially implementing the methodologies for power distribution monitoring, synthesis, or calculation based on several patents listing either of these entities as assignees [16, 17, 18, 19, 20, 21, 22, 23]. It is also worth noting that Toshiba is an assignee on a patent for a power distribution monitoring system with extensive methodological details for implementing neutron- and gamma-sensitive in-core detectors [24].

What is particularly unclear from existing documentation on implemented or patented power distribution inferencing methods is how effective, accurate, and robust they are across a range of implementation cases. A relatively limited body of literature presents some independent studies on a few methodologies, most of which are for very specific implementations.

One general method addressed in the literature is the use of weighting functions to relate the responses of the in-core or ex-core sensors to the power distributed in local segments of fuel. This methodology was adapted by foreign and domestic industry [25, 26]. Previous studies by the authors of this report have investigated how a weighting function–based method performs in the context of optical fiber-based gamma thermometers in theoretical [27] and university research reactors [28], as well as in the context of SPNDs in next-generation PWRs [29]. Note that a layer of sophistication was built into the methodology associated with these studies: an iterative process was implemented to ensure consistency among the working equations. In general, the weighting function–based methods appear to work well as long as the a priori knowledge of the reactor state is accurate and the system is not highly underspecified (e.g,. the number of sensors used for power inferencing is not extremely low compared to the number of fuel assembly segments for which local power is inferred).

Another method described in the literature is cubic spline synthesis (CSC), which has been used by nuclear power plants in South Korea [30]. Park conducted an independent study of this method in the context of 1,060 axial power distribution cases and found some instances of unreasonably high error [31]. Park also

tested the group method of data handling (GMDH) for axial power distribution synthesis, which involves an evolutionary algorithm designed to select the optimal representation of polynomial support functions; the comparison with CSC suggested that the GMDH method was more robust and less error prone, suggesting that CSC may not be the best method for industry implementation. Note that both CSC and GMDH methods have been only demonstrated for analysis of axial power distribution; their applicability to higher dimensional power distributions is unclear. It should also be noted that a Fourier series–based method has been implemented in legacy systems such as CECOR [15] to determine axial power distributions, but this method has received criticism because of its inability to handle certain axial power shapes [30, 32].

A few examples of more exotic methods for synthesizing reactor power distribution include the harmonics synthesis method, which was first formalized by Fu [32] and then was modified and tested by Kai [33]. The method is informed by ex-core detectors and is generally based on the notion that the power distribution is constructed of a linear combination of characteristic distribution functions; the detectors have response functions in accordance with each characteristic distribution. The method has been shown to be robust in the theoretical case of the High-Temperature-Reactor Pebble-bed Module across many different perturbation cases. Ramenazi has studied the nodal synthesis method, which is similar to the harmonics synthesis method. The nodal synthesis method uses in-core neutron detector readings [34], and power distribution is synthesized temporally by in-core detector readings and spatially by solving the neutron diffusion equation through a numerical harmonics calculation. This method showed low error in a simulated online reconstruction of the Bushehr Nuclear Power Plant reactor core. Finally, Shim demonstrated that using artificial neural networks can significantly reduce error in reconstruction of the axial power distribution in the Advanced Power Reactor 1400 in comparison to the Fourier series method [35].

Although a few conclusions may be drawn from the existing studies on power inferencing methods, in general, there are still many unknowns in this field of study, as considered below:

- For a given inferencing method in a given application, what is the optimal number and arrangement of in-core or ex-core sensors?
- Which methods tend to be more appropriate for certain applications as opposed to others?
- What is the comprehensive understanding of modifications and improvements which can be made to all methods in terms of their improved accuracy across a broad range of applications?
- What is the impact of sensor uncertainty on any given inferencing method across a broad range of applications?
- What types of functional limitations does each inferencing method have regarding the fidelity of the inferred power distribution?
- Which methods can be implemented at a faster calculation speed than others for a given application?
- When coupling the outputs of certain sensors into certain inferencing methods, are there certain sensor types or sensor specifications which can improve the accuracy of the inferred power distribution?

The list above is not exhaustive, but it does represent a few residual questions which still seem to remain regarding the field of nuclear reactor power distribution inferencing or synthesis. Studies that can begin to investigate even some of these questions will assist next-generation power reactor developers, as well as

operators of existing power reactors who may be interested in updating their operational systems, with making more well-informed decisions when deciding (1) which method would be most effective for a given reactor application, (2) which sensor type(s) and arrangement would be optimal, and (3) what type of performance can be expected based on simulation studies.

2 SCOPE OF STUDY

The general goal of this effort is to address unknowns regarding nuclear reactor power shape inferencing or synthesis as discussed in Section 1. Two studies have been devised to achieve this: (1) a study of the impact of SPND uncertainties when they are used to infer power distributions in next-generation PWRs, and (2) a high-fidelity study on perturbation detection in the Texas A&M Testing, Research, Isotopes, General Atomics Reactor (TAMU TRIGA). A weighting function based–method is being considered for both studies as implemented by the authors in earlier works [27, 28, 29]. Because iterative processes contain built-in layers of complexity, this approach has been coined the *point-based iterative* (PBI) method. It is crucial to define two terms which are used to describe neutronics calculations performed in this work: "homogeneous," and "heterogenous." In the context of this work, "homogeneous" neutronics calculations involve neutron flux tallying at a range of distances from a neutron source, which is representative of a single fuel assembly segment, and the surrounding medium is a single material which is the average composition of the heterogeneous core. "Heterogeneous" neutronics calculations involve neutron tally tracking from individual fuel assembly segments, to individual sensor locations, and the geometry of the core is divided into cells of appropriate sizes to be representative of the core in question.

The first-mentioned study leveraged neutronics models of the Westinghouse AP1000 and the NuScale Small Modular Reactor (SMR) which had been used in a previous study for power perturbation analysis in which the perturbations were induced by fissile material burnup [29]. The neutronics calculations are semi-heterogeneous, which in this case means that the a priori knowledge of the power distributions comes from fully heterogeneous geometries. However, the response functions used to calculate weighting functions are taken from simplified homogeneous reactor calculations. The in-core SPNDs are given some margin of uncertainty by allowing the current response of any SPND within the modeled reactor cores to randomly fall on a Gaussian distribution about some mean value informed by the priori power distribution, with a defined standard deviation. Using this general modeling framework, it is possible to analyze the impact of (1) varying the uncertainty (standard deviation) associated with the SPNDs and seeing the impact on the inferred power distribution error, (2) varying the number of SPNDs along the length of the axial detector strings in the core to see if increasing SPND density can reduce error, and (3) changing the fidelity of the calculation (e.g., the specificity of the calculation) to see if decreasing fidelity can decrease error, for example.

The second study leveraged a high-fidelity neutronics model of the TAMU TRIGA, a fully heterogeneous model suitable for use as a testbed for perturbation studies. The development of this model is described in detail in previous works [36, 37]. Because the model is fully heterogeneous, the neutron pathways used to inform response functions in the inferencing methodology are impacted by unique fuel/cladding boundary changes, cladding/water boundary changes, and control rods based on the source fuel segments and target sensor locations. In addition, inferencing codes used herein are adaptable to intake homogenously calculated response functions allowing for comparison with the fully heterogeneous model and assessment of the overall impact of the heterogeneities. In this work, the primary goal with the TAMU TRIGA model is to establish some baseline understanding of the error in inferring a perturbed power distribution for a

particular power distribution fidelity and in-core SPND arrangement.

Finally, in an effort to push toward more realistic power inferencing simulations, Geant4 (Geometry and Tracking), a Monte Carlo framework developed by CERN, was used to simulate realistic SPND current outputs based on total and incremental flux responses from individual fuel segments. In this analysis, the Geant4 model is of a generic SPND and was developed to aid in the creation of next-generation SPNDs for the Versatile Test Reactor project [38, 39]. The future goal is to integrate Geant4 models with all three aforementioned reactor cases in power inferencing simulations.

3 METHODOLOGY

3.1 Theory

The theoretical underpinnings of the PBI method considered herein, which is fundamentally a weighting function–based method relative to the literature, are explained in full detail in a previous report [29]. However, an abridged explanation of the mathematics is provided in this section. In some instances, a nuclear reactor core can be considered to have a true power distribution P^*, which comprises local fuel assembly segment power ($P^*_{A,z'}$) values where the index A corresponds to some given fuel assembly, and z' corresponds to an axial segment along the fuel assembly. Contrarily, there is also an assumed power distribution based on a priori knowledge of the reactor state in some instances, as denoted P, comprising $P_{A,z'}$ values. The goal is to obtain an inferred power distribution, $\langle P \rangle$, which comprises $\langle P_{A,z'} \rangle$ values. The $\langle P_{A,z'} \rangle$ values are calculated as

$$\langle P^*_{A,z'} \rangle = \frac{\sum_{S,z} (P^*_{A,z'})_{S,z} \Delta I_{A,z' \to S,z}}{\sum_{S,z} \Delta I_{A,z' \to S,z}}, \tag{1}$$

where $(P^*_{A,z'})_{S,z}$ is the estimated power in fuel assembly segment A, z', based on an SPND in the S sensor string at axial location z, and $\Delta I_{A,z' \to S,z}$ is the incremental current contribution from fuel assembly A, z' to SPND S, z. Equation (1) is thus a weighted average where each $(P^*_{A,z'})_{S,z}$ value is weighted by $\Delta I_{A,z' \to S,z}$ in determining $\langle P_{A,z'} \rangle$. Note that the total current in SPND S, z, is defined as

$$I_{S,z} = \sum_{A,z'} \Delta I_{A,z' \to S,z} \, , \tag{2}$$

and $(P^*_{A,z'})_{S,z}$ is defined as

$$(P^*_{A,z'})_{S,z} = I^*_{S,z} \frac{f_{A,z' \to S,z}}{R_{A,z' \to S,z}}. \tag{3}$$

In Eq. (3), $I^*_{S,z}$ is the simulated measured current at S, z in response to P^*, $R_{A,z' \to S,z}$ is a response function calculated from a full-core neutronics calculation, and $f_{A,z' \to S,z}$ is the fractional current in S, z which is a consequence of A, z', and it depends on $R_{A,z' \to S,z}$ [29]. Equation (1) must be solved iteratively because input of experimental (or simulated) $I^*_{S,z}$ values implies updates to $f_{A,z' \to S,z}$, which in turn affects $\langle P^*_{A,z'} \rangle$. Hence, the solution involves iterative updates to $f_{A,z' \to S,z}$ and $\langle P^*_{A,z'} \rangle$ until some convergence criterion is achieved.

The $\Delta I_{A,z' \to S,z}$ values can be calculated in a number of ways. If vanadium is considered to be the emitter material for the SPND, then $\Delta I_{A,z' \to S,z}$ can be calculated analytically:

$$\Delta I_{A,z' \to S,z} = V^{51} \sum_m \Delta \phi^m_{A,z' \to S,z} \sigma^{51}_{a,m} \, , \tag{4}$$

where V^{51} is the number of V-51 atoms present in the emitter, $\sigma^{51}_{a,m}$ is the neutron absorption cross section for V-51 averaged over energy bin m, and $\Delta\phi^{m}_{A,z'\rightarrow S,z}$ is the incremental flux in the mth energy bin from fuel assembly segment A, z' to SPND S, z. More complicated expressions may exist for other emitter materials with more complicated decay schemes, such as rhodium [40]. $\Delta\phi^{m}_{A,z'\rightarrow S,z}$ can be calculated in a homogeneous reactor neutronics calculation as long as the incremental flux can be characterized as a function of distance between A, z' and S, z for the heterogeneous reactor inferencing model. Conversely, $\Delta\phi^{m}_{A,z'\rightarrow S,z}$ can be calculated in a fully heterogeneous neutronics model, but it will require potentially >1 million neutron flux tallies and significant computation time to get reasonable statistics.

Contrary to analytical calculations, $\Delta I_{A,z'\rightarrow S,z}$ can be calculated through implementation of monte carlo particle transport codes such as Geant4, in which realistic sensor geometries and electron transport nuances can be considered. This is done by supplying $\Delta\phi^{m}_{A,z'\rightarrow S,z}$ values in some manner, either homogeneously or heterogeneously calculated. More details on Geant4 are captured in Section 6.

Finally, it is relevant to the work to consider the $I^{*}_{S,z}$ as potentially having experimental uncertainty. In that case we consider $I^{*}_{S,z}$ to be a normally distributed random variable, as defined by

$$I^{*}_{S,z} \sim \mathcal{N}(\mu^{*}_{S,z}, \sigma_{I^{*}_{S,z}}) \,, \tag{5}$$

where $\mu^{*}_{S,z}$ is the mean value of $I^{*}_{S,z}$, which reflects the error-free response to P^{*}, and $\sigma_{I^{*}_{S,z}}$ is the standard deviation of the normal distribution on which $I^{*}_{S,z}$ is based.

3.2 Code Implementation

The general framework describing how Python (version 3.9.7) scripts are implemented to process data from particle transport codes and simulate reactor power inferencing with SPNDs is shown in Fig. 1. If heterogeneous Monte Carlo N-Particle (MCNP) tallies are supplied, then the surface source read / surface source write (SSR/SSW) implementation is the considered MCNP method by which the $P_{A,z'}$ and $\phi^{m}_{A,z'\rightarrow S,z}$ values can be extracted. Based on a kcode calculation, the SSW card allows for tabulation of neutron tracks entering each fuel assembly segment A, z', which effectively provides normalized $P_{A,z'}$ values. The SSR card allows for neutron transport to be simulated from each A, z' location based on knowledge of the source distribution as determined from the SSW card. Then, using a volume flux average tally (F4 tally) for each sensor location, the $\phi^{m}_{A,z'\rightarrow S,z}$ can be calculated. The $P_{A,z'}$ tabulations and F4 tallies are converted into JSON files (or Python data dictionaries which function in a manner similar to JSON files) so that individual $P_{A,z'}$ and $\phi^{m}_{A,z'\rightarrow S,z}$ values can be corresponded with individual A, z' or S, z locations as value-key pairs.

The Reactor Geometries (RG) script stores geometry information for reactor models that are built into the codes in two separate classes: one for the arrangement of the fuel assembly segments, and one for the arrangement of sensors in the core. Attributes for the fuel assembly segment class include the centroid x and y locations of the fuel assemblies, the core height, and the core diameter or width. Attributes in the sensor class include x and y locations of the sensor strings and the number of sensors per string. The RG script is imported as a library to the power distributions (PD) script, which is responsible for calculating, storing, manipulating, and plotting reactor power distributions. Power distribution data are stored as multidimensional lists and are informed based on the aforementioned $P_{A,z'}$ JSON files. If $P_{A,z'}$ values are taken from literature and are not directly from Monte Carlo calculations, then $P_{A,z'}$ values can be hard-coded in the PD script.

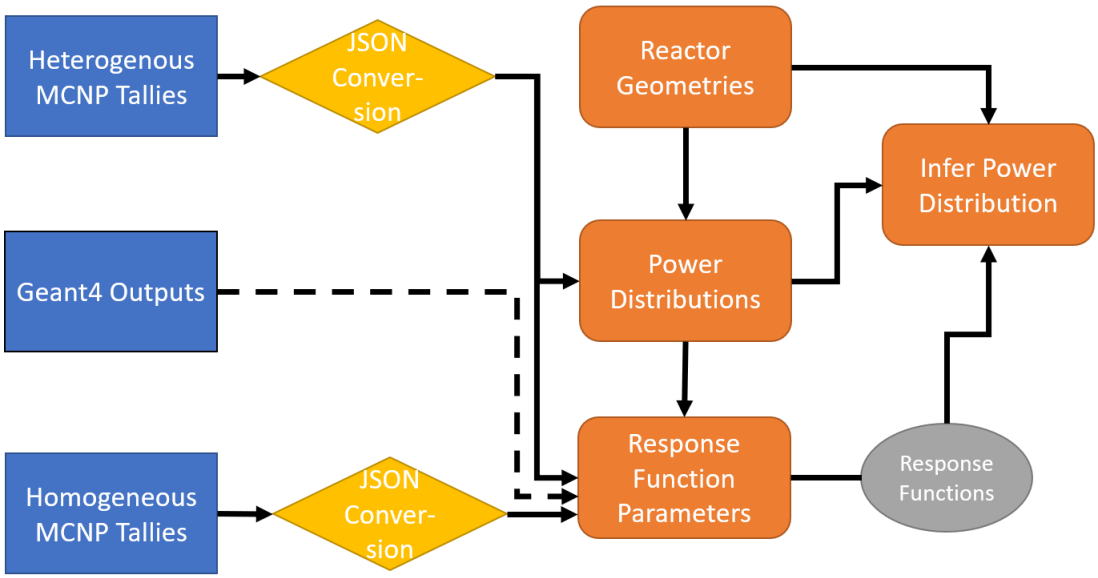

Figure 1. Flow diagram depicting the connection between sources of simulated reactor/sensor data and the Python scripts that process data and generate an inferred power distribution. (Blue boxes represent source data, yellow diamonds represent data formatting processes, orange boxes represent individual Python scripts, and gray circles represent processed data packages.)

The response function parameters (RFP) script is responsible for calculation of $R_{A,z'\to S,z}$ and $f_{A,z'\to S,z}$ for a given reactor model (where $R_{A,z'\to S,z}$ could represent the response of sensors to some perturbed condition, such as $R^*_{A,z'\to S,z}$). The RFP script has two custom classes: one for cross-section data of isotopes which may be used as emitters in SPNDs (imported from TENDL-2019 libraries), and one for sensor characteristics which actually defines the sensor arrangement in a reactor model. Object functions within the sensor characteristics class are responsible for reading the imported RG and PD stored data, as well as the $\phi^m_{A,z'\to S,z}$ values stored in JSON files. The object functions then calculate $R_{A,z'\to S,z}$ and $\Delta I_{A,z'\to S,z}$ values based on the arithmetic discussed in Section 3.1. If homogeneously calculated tally data are used, then the object functions determine distances between each A, z' and S, z location to determine $\phi^m_{A,z'\to S,z}$. The $R_{A,z'\to S,z}$ and $\Delta I_{A,z'\to S,z}$ are saved as NumPy arrays (version 1.24.1) and passed to the infer power distribution (IPD) script. The IPD script uses the $P_{A,z'}$ or $P^*_{A,z'}$ from the PD script, as well as the $R_{A,z'\to S,z}$ and $\Delta I_{A,z'\to S,z}$ NumPy arrays, to perform a power distribution inferencing calculation. Plots are generated based on the reactor geometry information stored in the RG script.

4 UNCERTAINTY ANALYSIS IN NEXT-GENERATION PWRs

4.1 Reactor Descriptions

The NuScale SMR is one of two next-generation LWRs serving as a testbed in this study to analyze the impact of SPND uncertainty on the inferencing of $\langle P^* \rangle$. It is a 250 MWt integral PWR with UO_2 fuel and a nominal operating pressure of 2,000 psia. It is intended to be one of multiple modules within a 4-, 6-, or 12-module pool-type reactor containment, respectively named VOYGR-4, -6, or -12 [41, 42]. The NuScale SMR is relatively small compared to traditional LWRs, with an active core height of 2.00 m and a diameter

of 1.50 m [43]. There are 37 fuel assemblies with SPND strings interstitially located in 12 of these fuel assemblies, with fuel enrichment levels as [44] shown in Fig. 2. Note that Fig. 2 shows beginning of life (BOL) conditions, and the enrichment levels change over the course of the core fuel cycle. In this work, only the BOL condition is considered, and assumed to represent the unperturbed power distribution P. It is not the focus of this particular study to see what happens to $\langle P^* \rangle$ when SPNDs respond to a perturbed distribution P^*; rather, in this study, SPNDs are responding to P with some level of Gaussian uncertainty, and they are yielding some $\langle P^* \rangle$, which is subject to sensor uncertainty. It is not clear what emitter material is intended for use in the NuScale SMR, but vanadium is assumed for this study. By design, the NuScale SMR is anticipated to have 4 SPNDs per sensor string, but a range of sensor string densities is considered in this analysis. Note that the power distribution in Fig. 2 is normalized to the maximum $P_{A,z'}$.

The Westinghouse AP1000 is the second of two next generation LWRs which served as an SPND uncertainty effects testbed. It is a 3400 MWt PWR with a nominal system pressure of 2,250 psi and sintered UO_2 fuel. It is considerably larger than the NuScale SMR, with an active core height of 4.27 m and a diameter of 3.04 m [45]. There are 157 fuel assemblies with SPND strings interstitially located in 42 of these fuel assemblies. Fuel enrichment levels are shown in Fig. 3. The enrichment levels [46] shown in Figs. 2 and 3 use the same color scale to facilitate comparison. Like with the NuScale SMR, the AP1000 power distribution considered herein is for BOL conditions. Sun indicates that the AP1000 uses SPNDs with vanadium emitters [47], so that is the emitter material considered. By design, the AP1000 includes 5 SPNDs per sensor string, but like the NuScale SMR analysis, a range of sensor string densities is considered herein. The distinct cross-hatching pattern from one assembly to another in P is clearly a feature of the cross-hatched enrichment pattern.

The TAMU TRIGA is a 900 kWt pool-type research reactor with TRIGA elements that allow for steady-state and pulsed reactor operation [36]. As part of the TRIGA reactor family, the TAMU TRIGA uses UZrH fuel with stainless-steel cladding [48]; by weight, the fuel is 30% U with a 20% ^{235}U enrichment level. Figure 4a shows a top-down depiction the TAMU TRIGA core (adapted from Parish [49]) indicating fuel element locations, instrumented fuel locations, and control rod locations. A cross-sectional, top-down view of the TAMU TRIGA core, as modeled in MCNP6 and visualized using MCNPX Visual Editor, is shown in Figure 4b, which also shows the 17 modeled locations for sensor strings. In this analysis, 4 SPNDs per sensor string are assumed, and for consistency, vanadium is the assumed emitter material. More details on the MCNP model are given in Section 5.1. The unperturbed power distribution P is shown in Figure 4c; however, as discussed in Section 5.2, an arbitrarily perturbed P^* is considered to analyze the accuracy with which the SPNDs infer the perturbation.

4.2 Sensor Uncertainty Implications

Both the AP1000 and NuScale SMR geometries were studied to determine the effect of ranging the SPND uncertainty. The study analyzed the impact this has on the error in the inferred power distribution. Namely, $\sigma_{I^*_{S,z}}$ was considered from a range of 1% to 10% of the nominal $I_{S,z}$ value, and the resultant error in the $\langle P_{A,z'} \rangle$ values were assessed. Standard SPND string densities were considered in this test: 4 equally spaced SPNDs per string in the NuScale SMR, and 5 equally spaced SPNDs per string in the AP1000. The inferred $\langle P \rangle$ distributions were determined with an axial fidelity of 5 equally sized segments for each fuel assembly. Although the $I^*_{S,z}$ are subject to simulated experimental uncertainty, they are in response to the unperturbed BOL power distribution; as such, any error observed in $\langle P_{A,z'} \rangle$ is solely because of the SPNDs operating with some level of uncertainty. In all calculations, the convergence criteria were such that the 2-norm of the residual between the most recent and second most recent iterations was 5×10^{-3}. Also, a relatively low

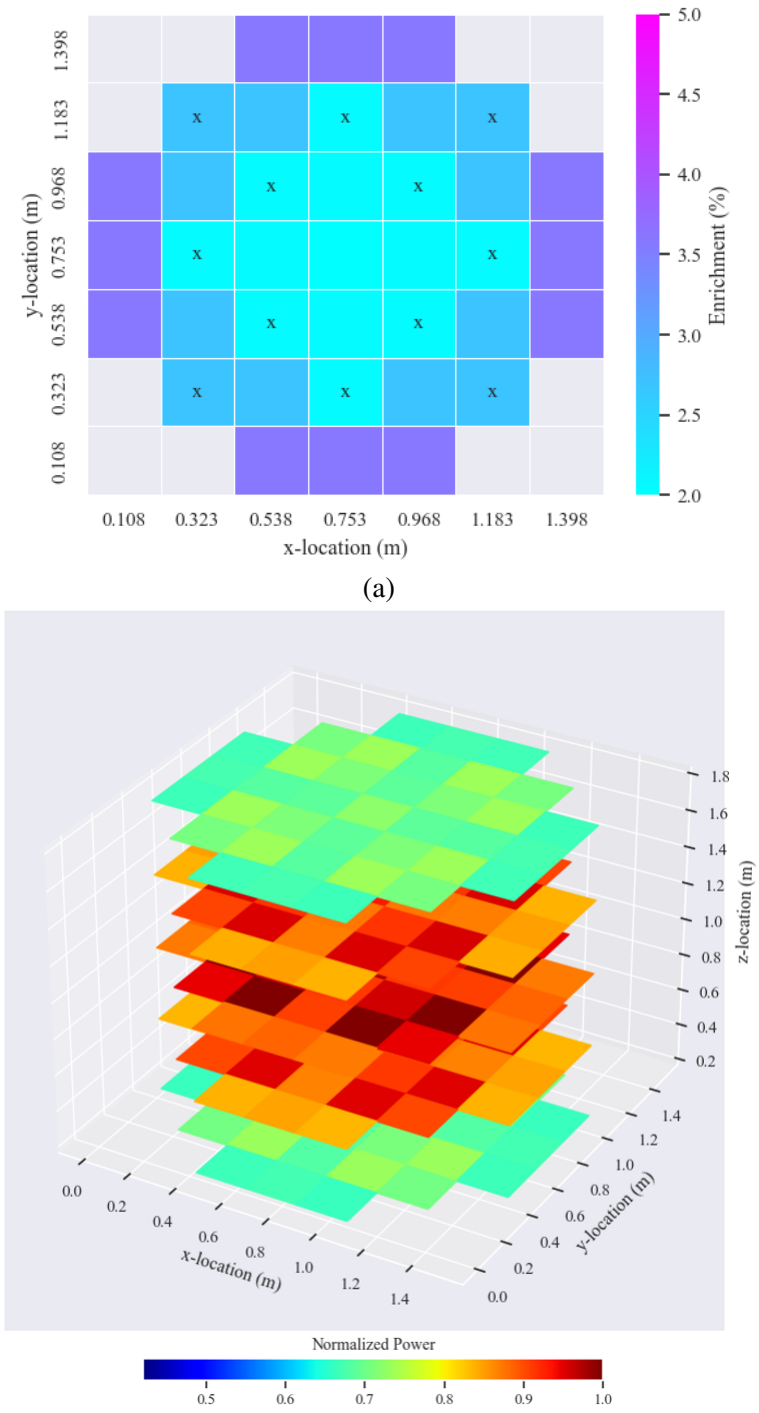

(a)

(b)

Figure 2. (a) Top-down view of the NuScale core geometry with ^{235}U enrichment values for each fuel assembly, and *x* marks for SPND string locations, (b) and the 3D normalized *P* distribution with 5 axial segments in the NuScale BOL core.

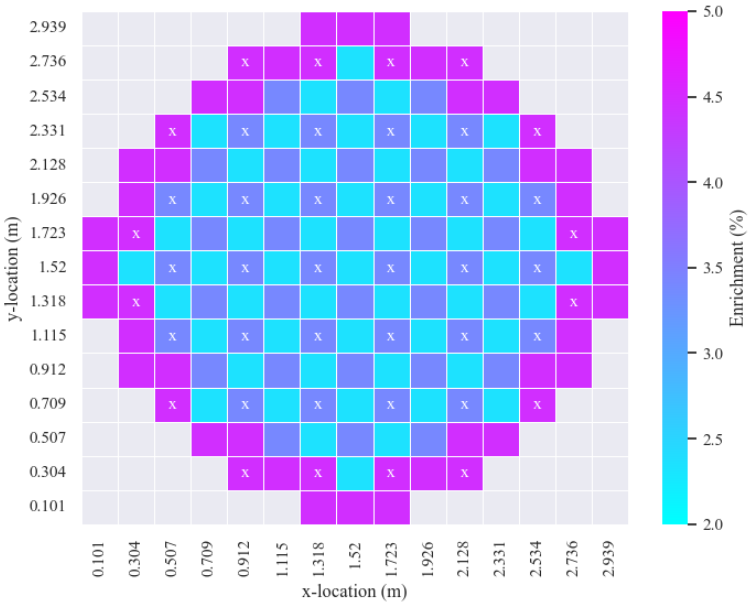

(a)

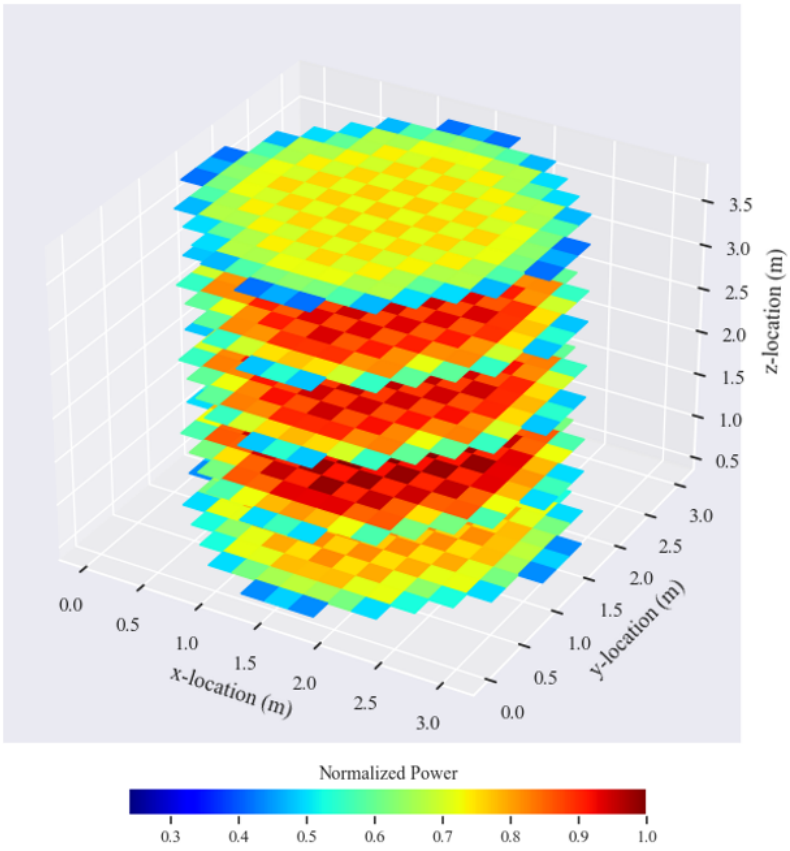

(b)

Figure 3. (a) Top down view of AP1000 core geometry with ^{235}U enrichment values for each fuel assembly, and *x* marks for SPND string locations, and (b) the 3D normalized *P* distribution with 5 axial segments in the AP1000 BOL core.

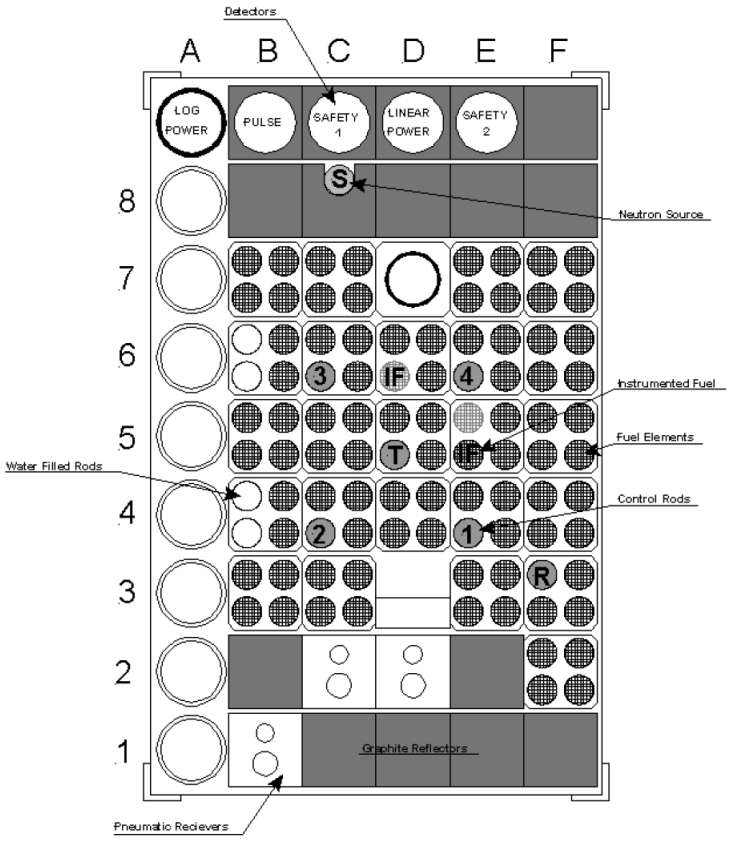

(a)

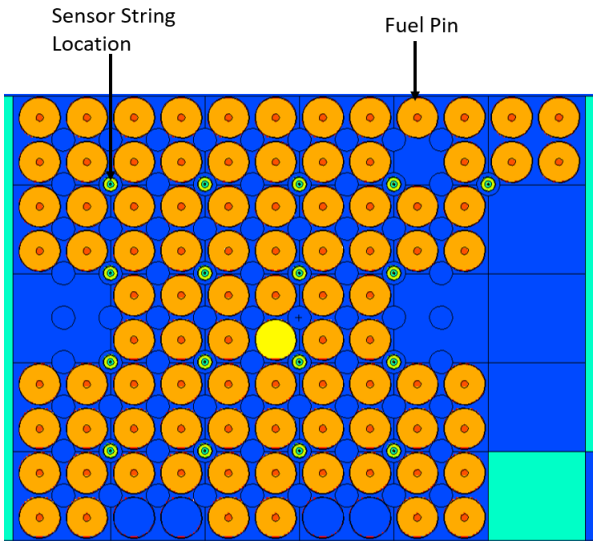

(b)

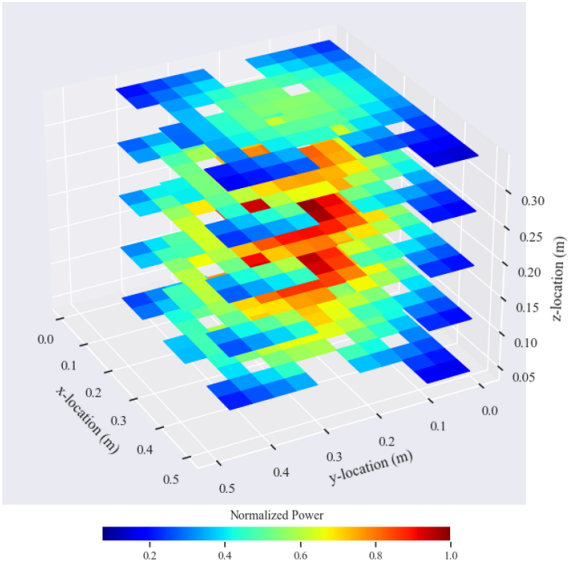

(c)

Figure 4. a) Top-down view of the TAMU TRIGA core [49], (b) MCNP cross-sectional image of the TAMU TRIGA core, (c) 3D normalized *P* distribution with 5 axial segments.

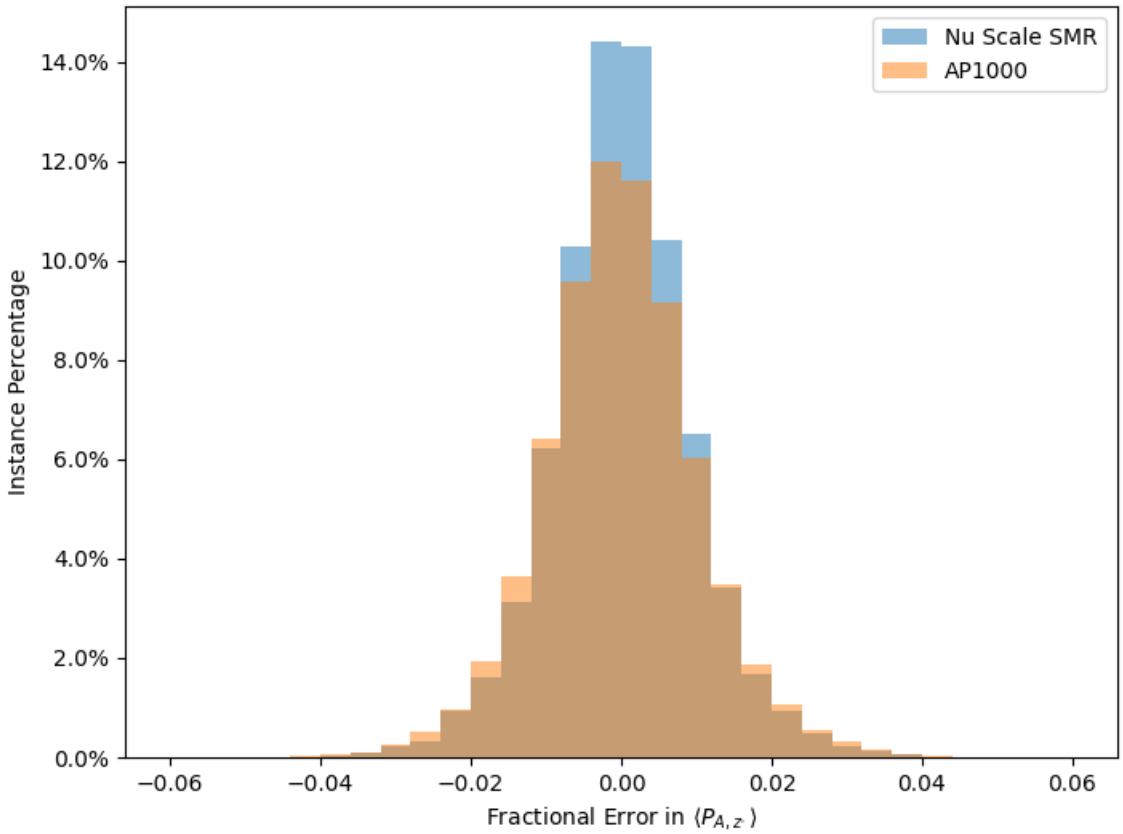

Figure 5. Distribution of fractional error in $\langle P_{A,z'} \rangle$ after 100 independent simulated SPND system measurements in the NuScale SMR and AP1000 with $\sigma(I^*_{S,z})$ values of 1%.

iteration limit of 30 iterations was established to prevent large runtime increases for diminishing returns.

Figure 5 shows the distribution of fractional error in $\langle P_{A,z'} \rangle$ for just 1% $\sigma_{I^*_{S,z}}$ specifically, after 100 independent simulated measurements with the entire SPND network in the core. This distribution is analogous to a real-world power monitoring system performing 100 core power synthesis calculations at some sampling rate R samples/min, so Fig. 5 represents the distribution of errors observed over time $t = 100/R$. The bins of the distribution are 0.2% wide, and the distribution shows the percent chance at which any $\langle P_{A,z'} \rangle$ value could fall into each of these error bins. As can be seen, both the NuScale SMR and the AP1000 show a distribution which is symmetrical about 0% error, so the error in $\langle P_{A,z'} \rangle$ does not preferentially skew toward positive or negative errors. The AP1000 shows slightly higher errors as indicated by the error distribution being slightly more spread out for the AP1000 vs. the NuScale SMR. However, results for both reactors indicate that no $\langle P_{A,z'} \rangle$ value seems to deviate from the true $P_{A,z'}$ value by more than 5%. Note that, based on the number of A, z' segments in both reactors, the sample sizes for the distributions in Fig. 5 are 18,500 instances for the NuScale SMR and 78,500 instances for the AP1000.

Figure 6 shows the impact of ranging $\sigma_{I^*_{S,z}}$ from 1% to 10% on both the average and maximum error in $\langle P_{A,z'} \rangle$. Ten independent simulated measurements with the entire SPND network in the core were conducted to generate the plots. As can be seen, average errors are reasonable across this range for both the

NuScale SMR and AP1000, scaling approximately with $\sigma_{I^*_{S,z}}$. However, maximum errors have the capacity to be significant if SPND uncertainty is not kept sufficiently low; maximum errors show the capacity to exceed 20% once $\sigma_{I^*_{S,z}}$ exceeds 5%. When comparing Figs. 5 and 6, it can be seen that the maximum errors in Fig. 6 represent the instances falling furthest from the center of the error distribution in Fig. 5. These high maximum error values represent particularly rare instances; however, it will be important that reactor control algorithms have the ability to handle rare, randomly high errors in $\langle P_{A,z'} \rangle$, which are a consequence of SPND uncertainty. If an SPND is yielding some particularly erroneous result and is not recognized as faulty, then the reactor could scram without just cause, assuming that scrams could be triggered by synthesized power distribution data. Although it is not the scope of this work to investigate methods of handling potentially high errors in SPND outputs which may occur at some low frequency, fault and failure detection and handling are the focus of several published studies [50, 51, 52, 53]. The work conducted herein suggests that it is crucial to implement some form of fault detection and diagnostics if SPND uncertainties are expected to exceed more than 1–2 %. Of course, there may be ways in which the inferencing method or sensor arrangement could be altered, or optimized to reduce the maximum error in $\langle P_{A,z'} \rangle$ associated with some $\sigma_{I^*_{S,z}}$.

4.3 Sensor String Density Implications

A similar study was conducted with both the AP1000 and NuScale SMR as that described in Section 4.2, except that $\sigma_{I^*_{S,z}}$ was held constant at 1%, and each SPND string was varied in terms of its sensor density from 3–10 SPNDs per string. As described in Section 4.2, the inferred $\langle P \rangle$ distributions were determined with an axial fidelity of 5 equally sized segments for each fuel assembly. Unlike the relatively obvious relationship between $\sigma_{I^*_{S,z}}$ and errors in $\langle P_{A,z'} \rangle$, the relationship between sensor string density and errors in $\langle P_{A,z'} \rangle$ is more complicated.

The average and maximum errors in $\langle P_{A,z'} \rangle$ for the NuScale SMR are shown in Figs. 7a and 7c. There is a slight reduction in both types of error as a function of increasing sensor string density. However, this relationship is slight. The average and maximum errors in $\langle P_{A,z'} \rangle$ for the AP1000 are shown in Figs. 7b and 7d, indicating particularly high errors for SPND string densities of 7 and 9 SPNDs per string. In general, these error plots suggest that increasing the number of SPNDs per string does not obviously reduce errors in $\langle P_{A,z'} \rangle$, and in some cases it may actually result in an increase in error. This may be a pertinent consideration for next-generation reactor developers who are intending to optimize the SPND arrangements in core designs.

It is important to note that these calculations were performed with an iteration limit, and Figs. 7e and 7f show that there are certain SPND string densities susceptible to reaching this iteration limit for the NuScale SMR and the AP1000, respectively. The dark boxes indicate simulation cases in which the iteration limit was reached, and the light boxes indicate that convergence was achieved before the iteration limit. In fact, Fig. 7.f indicates that the entire band from 6–9 SPNDs per string consistently results in the iteration limit being reached for the AP1000. It is possible that higher iteration limits could result in a more noticeable reduction in errors in $\langle P_{A,z'} \rangle$ for denser SPND strings; this could be investigated in a future study. However, particularly high iteration limits may not be feasible if reactor operators require high acquisition rates for updated syntheses of the reactor core power distribution.

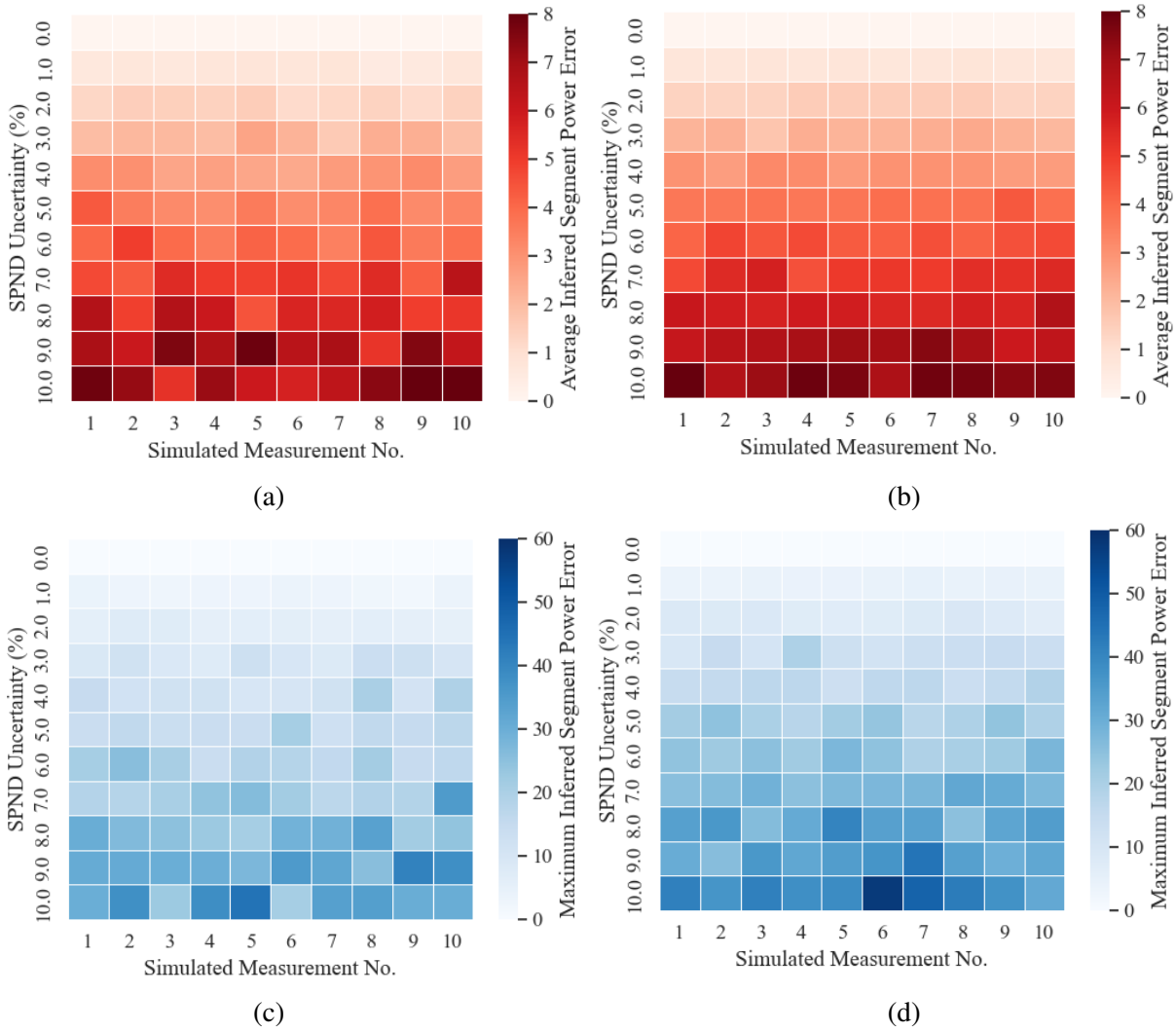

Figure 6. Average error in $\langle P_{A,z'} \rangle$ over 10 independent simulated SPND system measurements for varying $\sigma(I^*_{S,z})$ in (a) NuScale SMR and (b) AP1000. Maximum error in $\langle P_{A,z'} \rangle$ over 10 independent simulated SPND system measurements for varying $\sigma(I^*_{S,z})$ in (c) NuScale SMR and (d) AP1000.

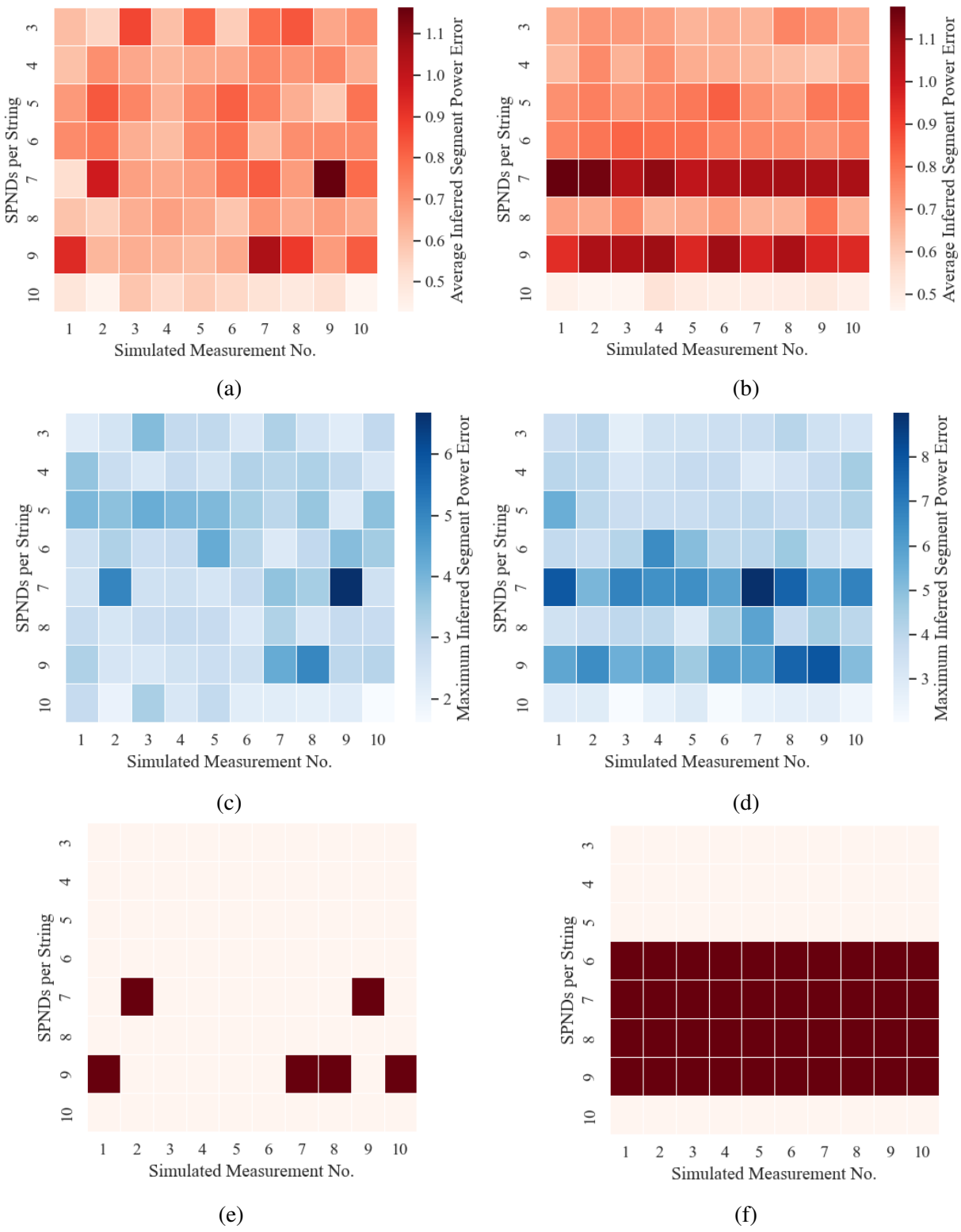

Figure 7. Average error in $\langle P_{A,z'} \rangle$ over 10 independent simulated SPND system measurements for varying SPND string densities in (a) NuScale SMR and (b) AP1000. Maximum error in $\langle P_{A,z'}$ for these same simulations for (c) NuScale SMR and (d) AP1000. Indication of iteration limit being reached for these same simulations for (e) NuScale SMR and (f) AP1000.

5 HIGH FIDELITY MODEL CASE: TAMU TRIGA

5.1 MCNP Model

The MCNP model of the TAMU TRIGA was generated following the described SSR/SSW logic in Section 3.2. The TAMU TRIGA fuel was divided into segments on the pin level so that each individual fuel pin was divided into 15 1-inch segments, covering the total effective core height of 15 inches. A k-code calculation was performed with the SSW card activated, with each of the 1,290 fuel pin segments specified for which a surface source file that needed to be generated. Each of these source files was run separately for each of the 1,290 fuel pin segments. A flexible tally scheme was devised to allow for both gamma- and neutron-sensitive sensors to be considered, with a range of sensor string densities to be considered. This was accomplished by implementing sensor strings divided into 1-inch axial segments that were centered at points from the top of the effective core to the bottom of the effective core (i.e., 16 total potential sensor locations per string), using f4 tallies for neutron flux and gamma-ray flux. For the total number of potential sensor locations, this resulted in a sum total of 701,760 tallies (half of which were neutron flux tallies) which were tracked over the 1290 SSR runs, such that each f4 tally represents one the sum $\sum_m \Delta\phi^m_{A,z'\rightarrow S,z}$. The individual $\Delta\phi^m_{A,z'\rightarrow S,z}$ values corresponding to energy bins centered at values ranging from ~10^{-11}–20 MeV were determined homogeneously following the same process outlined in Birri et al. [29].

An example of a tally calculation of $\sum_m \Delta\phi^m_{A,z'\rightarrow S,z}$ (after analytical conversion into $\Delta I_{A,z'\rightarrow S,z}$) is shown in Fig. 8. The top left and right side images show the top-down and cross-sectional views of the MCNP model, where the cross-sectional view is labeled with a red dashed line in the top-down view. The bottom left plot shows the normalized $\Delta I_{A,z'\rightarrow S,z}$ from the entire core to a particular sensor location in question. The location of the sensor location in question (i.e. SPND) is outlined in pink dotted lines in the top-down and cross-sectional views of the MCNP model and is represented as a pink cylinder in the bottom left plot; the corresponding sensor string is indicated by a green dashed line. In general, the plot shows that $\Delta I_{A,z'\rightarrow S,z}$ decreases exponentially as a function of distance from the sensor location, which is anticipated because of the $1/r^2$ dependence on neutron flux when neutrons are isotropically emitted from a point source (where r is distance from the point source), and also because of the exponential nature of neutron attenuation in matter.

5.2 Validation and Perturbation Studies

To test the ability to perform an accurate power synthesis with the high-fidelity TAMU TRIGA model, two tests were conducted with one particular sensor-core geometry. In Test 1, the true power distribution to which the sensors were responding was exactly equal to the assumed unperturbed power distribution (i.e., $P^* = P$). In Test 2, the true power distribution was perturbed such that a localized peak in the power distribution was defined and the synthesized power distribution relied on the perturbed SPND responses (I^*). In both cases, the power distribution was resolved on a pin-by-pin level in the x-y plane with 5 axial segments in z. SPND strings were assumed to exist in all 17 string locations in the core, with 4 equally spaced SPNDs per string. The convergence criteria for both tests was such that the 2-norm of the residual between the most recent and second most recent iterations was 1×10^{-3} with no specified iteration limit.

In Test 2 of the TAMU TRIGA, the local perturbation was assumed to be centered on the instrumented fuel rod in fuel element D6, as shown in Fig. 4a. The perturbation is assumed to take on a normal distribution with a 2D normal vector $\boldsymbol{V}$ defined as

$$\boldsymbol{V} \sim \mathcal{N}(\boldsymbol{\mu}, \boldsymbol{\Sigma}) \,, \tag{6}$$

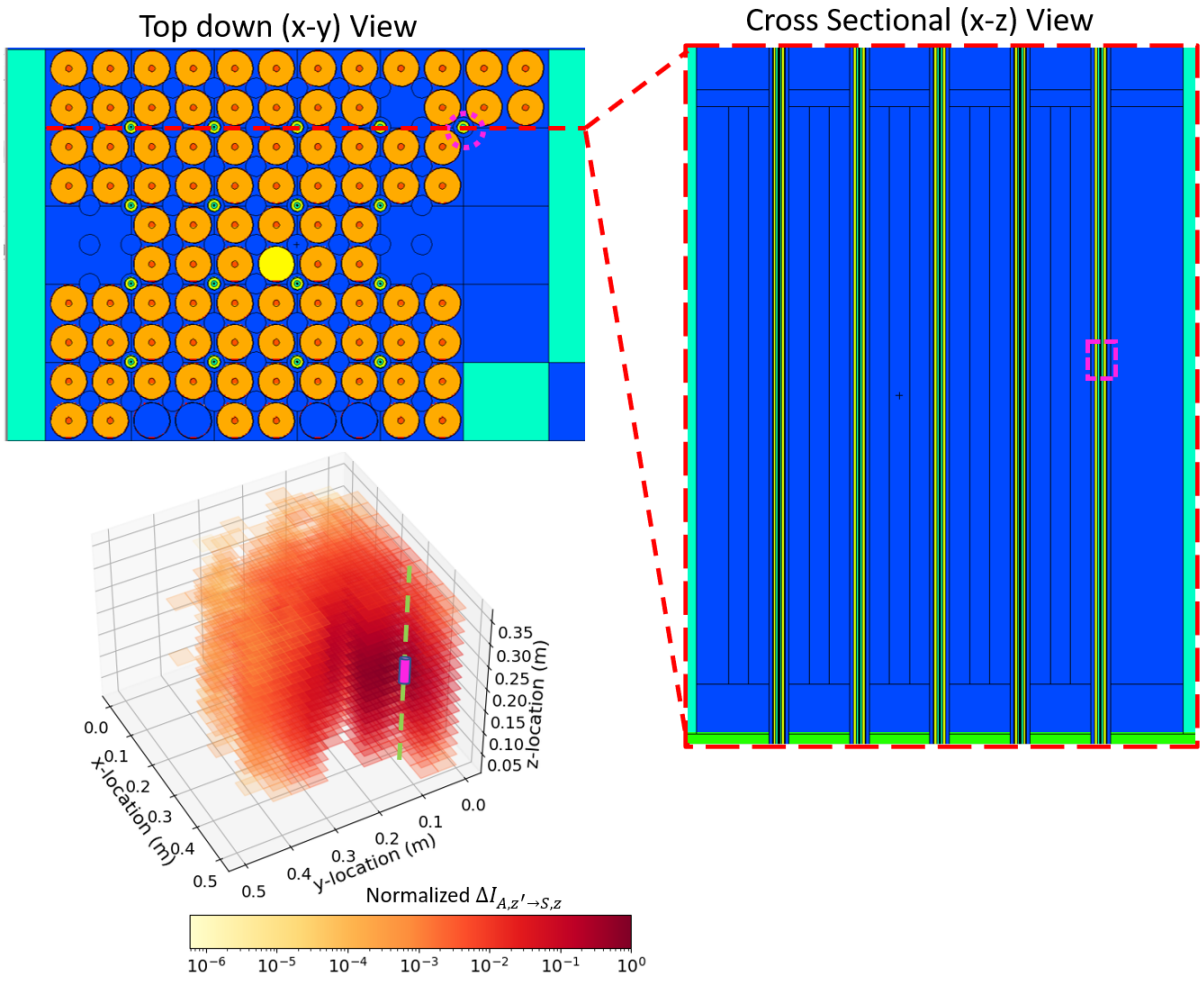

Figure 8. $\Delta I_{A,z' \to S,z}$ **as modeled in the TAMU TRIGA MCNP model from all fuel pin segments to a single sensor location (pink). Top left and right side images are taken directly from the model in the MCNPX Visual Editor; the bottom left image was generated in python using the package Matplotlib version 3.5.1.**

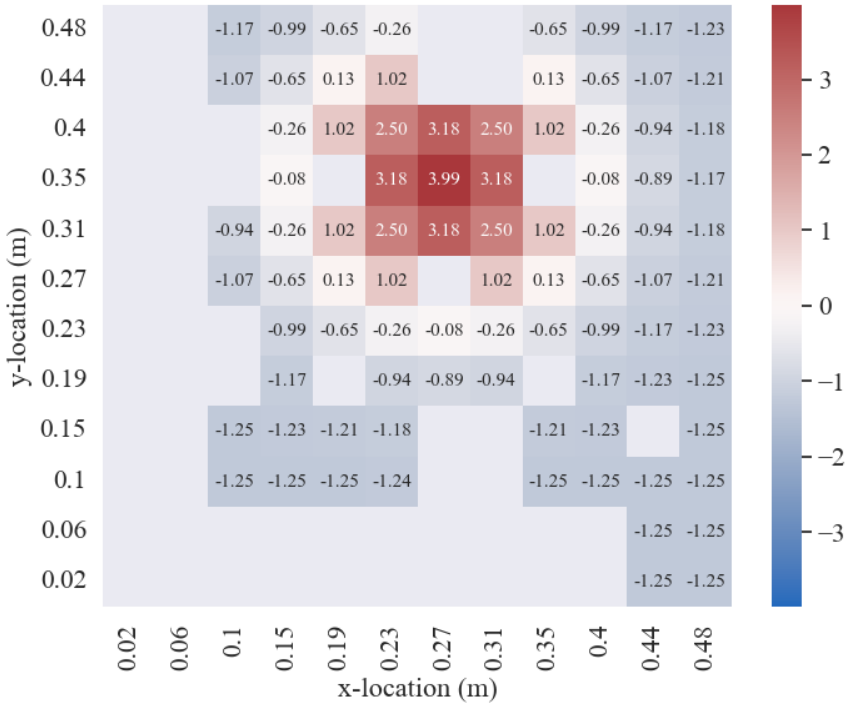

Figure 9. Percent difference between the axial $P*$ and P in the perturbation test of the TAMU TRIGA (Test 2).

where

$$\boldsymbol{\mu} = \begin{bmatrix} \mu_x \\ \mu_y \end{bmatrix} \tag{7}$$

and

$$\boldsymbol{\Sigma} = \begin{bmatrix} \sigma_x^2 & 0 \\ 0 & \sigma_y^2 \end{bmatrix}. \tag{8}$$

In Eqs. (7) and (8), μ_x and μ_y are the x and y location where the normal distribution is centered (in this case, the centroid of the instrumented fuel rod in element D6), and σ_x^2 and σ_y^2 are the variance of the distribution in the x and y axes. In this study, $\sigma_x^2 = \sigma_y^2 = 0.125$ m. Defining the probability density function of $\boldsymbol{V}$ as $f_V(x_{A,z'}, y_{A,z'})$, where $x_{A,z'}$ and $y_{A,z'}$ are the respective x and y locations of some fuel pin A, z', the perturbed power distribution for this TAMU TRIGA test is defined as

$$P^* \ni P^*_{A,z'} = \frac{P_{A,z'} + P_{A,z'} f_V(x_{A,z'}, y_{A,z'})}{\sum_{S,z} P_{A,z'} + P_{A,z'} f_V(x_{A,z'}, y_{A,z'})}. \tag{9}$$

A plot of the radial distribution of the percent difference between $P^*_{A,z'}$ and $P_{A,z'}$ is shown in Fig. 9.

Regarding the results of Test 1, the convergence criteria were met within one iteration, which is expected for the case in which $P^* = P$ [29]. Simply put, Test 1 serves to demonstrate that the integration between the TAMU TRIGA MCNP model and the inferencing codes is a valid and functional connection. The final 2-norm of the residual between $\langle P^* \rangle$ and P was 7.88×10^{-15}, which is on the order of machine precision.

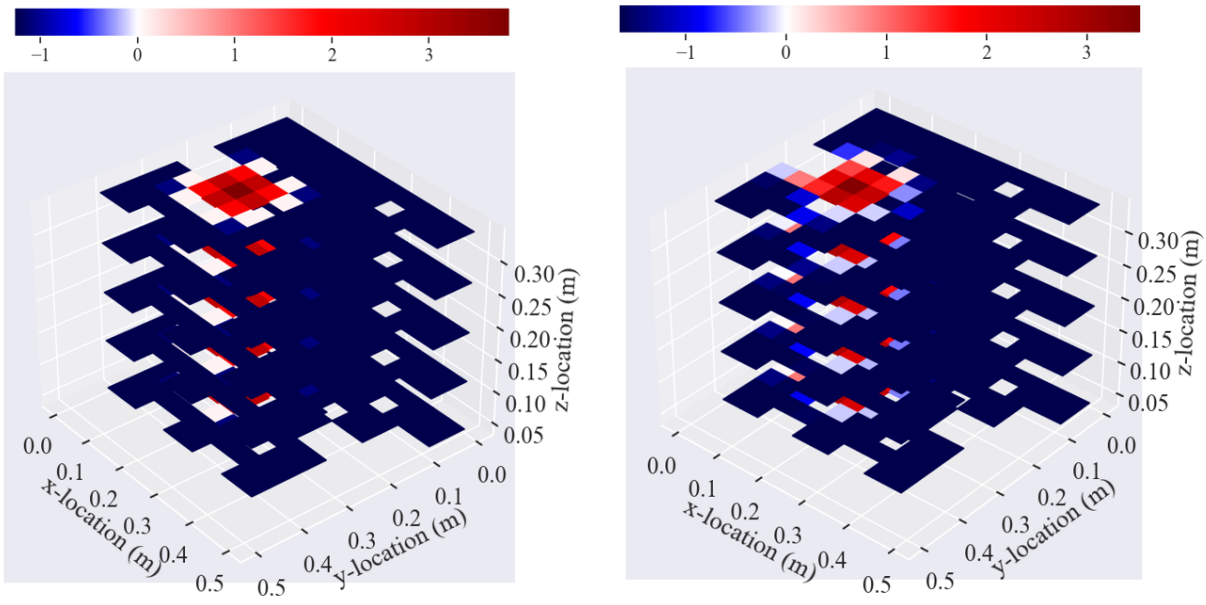

(a) (b)

Figure 10. Percent discrepancy between (a) $P*$ and P, and (b) $\langle P^* \rangle$ and P for Test 2 of the TAMU TRIGA.

In general, Test 1 yields confidence that the code is working properly based on the nearly identical distributions of $\langle P^* \rangle$ and P.

Regarding the results of Test 2, the plots of the percent discrepancy between $P*$ and P, as well as between $\langle P^* \rangle$ and P, are shown in Fig. 10: Fig 10a shows the percent discrepancy between the true perturbed and assumed unperturbed distributions, whereas Fig 10b shows the percent discrepancy between the simulated inferred and assumed unperturbed distributions. In general, it is clear that the simulated SPND response results in the ability to localize the perturbation as being centered on the appropriate fuel pin, with an appropriate spatial profile and magnitude. Of course, the inferred perturbation is not without error, which is in part caused by a finite residual defined as the convergence criteria, and also the under-specificity of the calculation (i.e., there are more unknowns, $\langle P^*_{A,z'} \rangle$ values, than knowns, $I^*_{S,z}$ values). Nevertheless, the errors are rather low, with the average error in $\langle P^*_{A,z'} \rangle$ being 0.19 %, and the maximum error in $\langle P^*_{A,z'} \rangle$ being 1.4 %.

6 GEANT4 INTEGRATION

6.1 Model Details

The input to the Geant4 model, which is considered for integration in the power synthesis simulation workflow, was twofold. The first input was a vanadium SPND with an emitter radius of 2.54 mm and 10 mm long. The insulator was magnesium oxide and 0.25 mm thick, and the collector was 0.25 mm thick Inconel steel. The second input to the model was a neutron spectrum from a given fuel segment inside the nuclear reactor provided by an MCNP model of the homogeneous representation of a given nuclear reactor core. A total of 200 unique distances between fuel segment and SPND were captured, so the Geant4

simulation was run 200 times to appropriately simulate each segment's contribution to the overall SPND signal. Each simulation was run with 2E8 events to provide sufficient statistics. The chosen output of the simulation was the number of electrons generated in the emitter which is proportional to the total current generated by an SPND. This output was chosen over the number of electrons that entered the emitter because this SPND was not optimized for this reactor's neutron spectrum and therefore would introduce systematic error to the results.

6.2 Initial Results with NuScale

For the NuScale SMR homogenized MCNP model, the normalized $\Delta I_{A,z' \rightarrow S,z}$ as a function of distance between A, z' and S, z are shown in Fig. 11 for both the Geant4 SPND model and the analytical model which has been considered previously. Note that in both cases, the normalized $\Delta I_{A,z' \rightarrow S,z}$ is determined based on supplying $\phi^m_{A,z' \rightarrow S,z}$ values to both models. Fig. 11 also shows the number of electrons emitted per source particle (i.e., neutrons) in the Geant4 modeled sensor as a function of distance between A, z' and S, z. As expected, this number generally increases as the distance between A, z' and S, z increases. This is because the neutrons are proportionally more thermalized as this distance increases, which in turn increases the likelihood of absorption by V-51 based on its cross-section as a function of neutron energy.

Fig. 11 clearly indicates that the magnitude of $\Delta I_{A,z' \rightarrow S,z}$ between the analytical and Geant4 SPND models differs significantly for most distances between A, z' and S, z, except perhaps for when A, z' and S, z are particularly close (within 0.05 m). Relatively speaking, this means that the $I_{S,z}$ in the Geant4 modeled SPND will be primarily be comprised of contributions from particularly close fuel assembly segments in comparison to the analytical model. This makes physical sense because the fast neutron peak in the $\phi_{A,z' \rightarrow S,z}$ energy spectra diminishes rapidly as the distance between A, z' and S, z increases [29]. This means that self-shielding effects are more significant in a sensor with finite geometry, thereby diminishing the $\Delta I_{A,z' \rightarrow S,z}$ values.

The impact this will have on the inferred power distribution in a variety of sensor-core configurations is still under investigation. Logically, it can be concluded that the response functions for short distances between A, z' and S, z will become relatively high, and for long distances between A, z' and S, z, it will become relatively low when a Geant4 model is considered as opposed to an analytical model. Such a trend could have implications for fuel segments of the core which are particularly far from any SPND in that a perturbation in such fuel segments may be more difficult to detect. The Geant4 data in Fig. 11 are only for one particular SPND geometry and material selection; the resultant $\Delta I_{A,z' \rightarrow S,z}$ values could be closer to the analytical model as a result of strategic design decisions to reduce the extent to which self-shielding could be occurring in the SPND.

7 CONCLUSION

It is clear that the existing domestic nuclear reactor fleet uses power synthesis methods based on the responses of in-core and ex-core neutron flux and gamma-ray flux sensors. Next-generation LWRs—and likely other advanced reactor designs—must use similar methods to allow for an accurate, high-fidelity understanding of the progression of the 3D power distribution in the core throughout the operational lifecycle. Becuse studies in the field of power distribution synthesis are limited, many questions remain regarding optimization strategies, implications of uncertainty, error-reduction improvements, synthesis code runtime increases and tradeoffs, and versatility with varying sensor types. This report has addressed some of these questions in part for specific cases. One analysis herein on SPND uncertainty in the NuScale

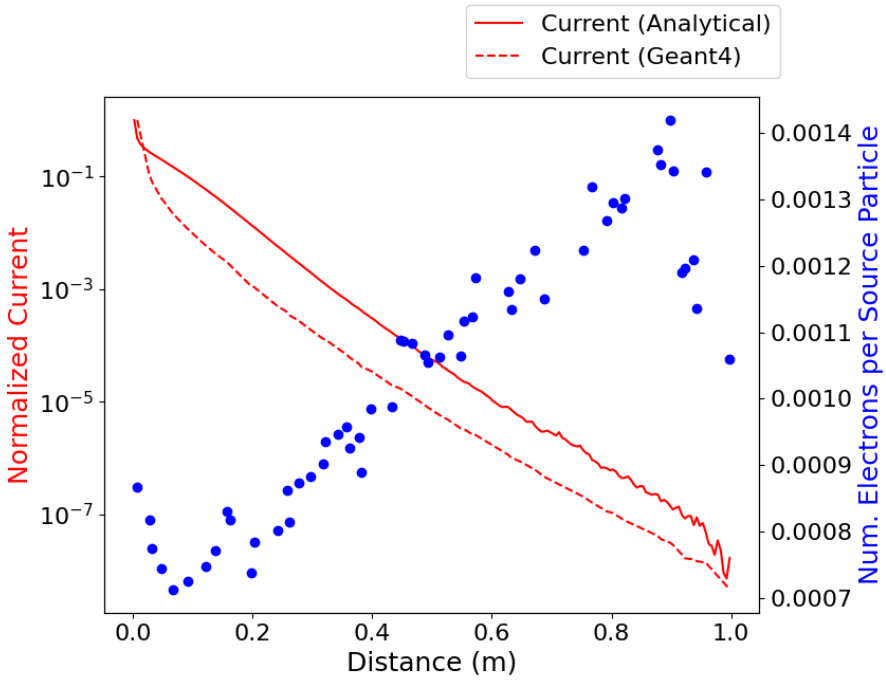

Figure 11. Normalized $\Delta I_{A,z' \to S,z}$ as a function of distance between A, z' and S, z for both the Geant4-modeled SPND and the analytically modeled SPND. The number of electrons per source particle (neutrons) in the Geant4 model are also plotted.

SMR and the Westinghouse AP1000 has revealed that, with increasing random uncertainty in the SPND readings, the average error in the synthesized power distribution can be kept to reasonable levels, but the maximum error can be considerably high (>15 %) if the SPND uncertainty is >3%. Therefore, it is crucial that measures are taken to minimize SPND uncertainties through careful sensor design and development of sensor outlier detection algorithms. This same analysis of sensor uncertainties also revealed that there is minimal, if any, reduction to the error in the synthesized power distribution when the number of SPNDs per sensor string is increased from 3 to 10; reactor developers may be able to use this information when determining the number of SPNDs in the core design. Another analysis herein on power distribution perturbation detection in a high-fidelity simulation of the TAMU TRIGA reactor revealed that it was indeed possible, given a particular configuration of SPNDs, to accurately infer a localized perturbation which peaks in a particular fuel pin, giving confidence in the overall methodology in this modeling case with particularly accurate sensor response functions, and providing a starting point for continued parameterization of perturbation analysis to assess overall limits. Finally, initial results of current outputs in a Geant4 modeled SPND, in comparison to analytically modeled SPND, reveal large discrepancies, suggesting that Geant4 models (which include realistic sensor geometries) should be considered in future simulation studies to account for realistic sensor physics.

8 REFERENCES

References

[1] Mercier, Bertrand, Ziliang, Zeng, Liyi, Chen, and Nuoya, Shao. Modeling and control of xenon oscillations in thermal neutron reactors. *EPJ Nuclear Sci. Technol.*, 6:48, 2020.

[2] Abhishek Chakraborty, M. P. S. Fernando, and A. S. Pradhan. Performance of flux mapping system during spatial xenon induced oscillations in PHWRs. In Manaswita Bose and Anish Modi, editors, *Proceedings of the 7th International Conference on Advances in Energy Research*, pages 1559–1570, Singapore, 2021. Springer Singapore.

[3] Petra Mala, Hakim Ferroukhi, Alexander L. Vasiliev, Marcus Seidl, and Denis Janin. Bowing effects on power and burn-up distributions for simplified full PWR and BWR cores. In *International Conference on Mathematics and Computational Methods Applied to Nuclear Science and Engineering*, Jeju, Korea, 2017.

[4] Jinfeng Li. Monte Carlo investigation of the UK's first EPR nuclear reactor startup core using Serpent. *Energies*, 13(19), 2020.

[5] Aiman Dandi, MinJae Lee, and Myung Hyun Kim. Feasibility of combinational burnable poison pins for 24-month cycle PWR reload core. *Nuclear Engineering and Technology*, 52(2):238–247, 2020.

[6] Foad Mehdi Zadeh, Stéphane Etienne, Richard Chambon, Guy Marleau, and Alberto Teyssedou. Effect of 3-d moderator flow configurations on the reactivity of candu nuclear reactors. *Annals of Nuclear Energy*, 99:136–150, 2017.

[7] Mina Torabi, A. Lashkari, Seyed Farhad Masoudi, and Somayeh Bagheri. Neutronic analysis of control rod effect on safety parameters in tehran research reactor. *Nuclear Engineering and Technology*, 50(7):1017–1023, 2018.

[8] T. Morita C. L. Beard. Beacon - core monitoring and operations support system, 1994. WCAP-12472-P-A.

[9] T. Morita. Beacon - core monitoring and operations support system, 2000. WCAP-12472-P-A Addendum 1-A.

[10] W. A. Boyd. Beacon - core monitoring and operations support system, 2002. WCAP-12472-P-A Addendum 2-A.

[11] T. Morita W. A. Boyd, M. A. Book. Beacon - core monitoring and operations support system, 2004. WCAP-12472-P-A Addendum 3-A.

[12] D. J. Krieg W. A. Boyd. Beacon - core monitoring and operations support system, 2010. WCAP-12472-P-A Addendum 4-A.

[13] General Electric Company. Methodology and uncertainties for safety limit mcpr evaluations, 1999. NEDO-32601-A Revision 0.

[14] Global Nuclear Fuel. Supporting discussion, information and gestar ii markups. non-proprietary information– class i (public), 2016. MFN 16-011. Enclosure 2.

[15] WB Terney, JL Biffer, CO Dechand, A Jonsson, and RM Versluis. The CE CECOR fixed in-core detector analysis system. *Trans. Am. Nucl. Soc.;(United States)*, 44(CONF-830609-), 1983.

[16] Yasuo Nishizawa. Reactor power control apparatus, 1982. US Patent 4,333,797A.

[17] Albert Joseph Impink Jr. Method and apparatus for continuous on-line synthesis of power distribution in a nuclear reactor core, 1987. US Patent 4,637,910A.

[18] Albert Joseph Impink Jr. and Louis Richard Grobmyer. Method and apparatus for continuous on-line synthesis of power distribution in a nuclear reactor core, 1988. US Patent 4,774,049A.

[19] Albert Joseph Impink Jr. Axial power distribution monitor and display using outputs from ex-core detectors and thermocouples, 1988. US Patent 4,774,050.

[20] Albert Joseph Impink Jr. and Louis Richard Grobmyer. A method and apparatus for continuous nuclear power distribution synthesis, 1989. EP0323280A2.

[21] Albert Joseph Impink Jr. and Louis Richard Grobmyer. Continuous, online nuclear power distribution synthesis system and method, 1989. US Patent 4,839,134A.

[22] Michael D. Heibel. Method and a system for accurately calculating pwr power from excore detector currents corrected for changes in 3-d power distribution and coolant density, 1996. US Patent 5,490,184A.

[23] Masaki Kaneda Keiji Suzuki Atsushi Fushimi, Yuji Ichinose. Monitoring control system of nuclear power plant, 2011. JP2012233705A.

[24] Koji Hirukawa, Shungo Sakurai, and Takafumi Naka. Nuclear reactor power distribution monitoring system and method including nuclear reactor instrumentation system, 2001. US Patent 6,236,698B1.

[25] William A Boyd and R Wade Miller. The beacon on-line core monitoring system: functional upgrades and applications. In *Proc. Specialists' Meeting "In-core instrumentation and core assessment*, 1996.

[26] Masayuki Tojo, Takafumi Naka, Tatsuya Iwamoto, Junichi Koyama, and Kenichi Harada. Application of the new core monitoring system,'GNF-ARGOS', to the start-up tracking calculation of abwr. 2008.

[27] Anthony Birri and Thomas E. Blue. Methodology for inferring reactor core power distribution from an optical fiber based gamma thermometer array. *Progress in Nuclear Energy*, 130:103552, 2020.

[28] Anthony Birri. *The Development of an Optical Fiber Based Gamma Thermometer*. PhD thesis, Ohio State University, 2021.

[29] Anthony Birri, Daniel C Sweeney, and N Dianne Bull Ezell. Simulating self-powered neutron detector responses to infer burnup-induced power distribution perturbations in next-generation light water reactors. *Progress in Nuclear Energy*, 153:104437, 2022.

[30] Wang-Kee In, Hyung-Keun Yoo, Geun-Sun Auh, Chong-Chul Lee, and Si-Hwan Kim. Application of cubic spline synthesis in on-line core axial power distribution monitoring. *Nuclear Engineering and Technology*, 23(3):316–320, 1991.

[31] Moon-Ghu Park and Ho-Cheol Shin. Reactor power shape synthesis using group method of data handling. *Annals of Nuclear Energy*, 72:467–470, 2014.

[32] Li Fu, Luo Zhengpei, and Hu Yongming. Harmonics synthesis method for core flux distribution reconstruction. *Progress in Nuclear Energy*, 31(4):369–372, 1997.

[33] Fan Kai, Li Fu, Zhou Xuhua, and Guo Jiong. Improved harmonics synthesis method and its application in reconstructing power distribution of htr-pm. *Nuclear Engineering and Design*, 355:110351, 2019.

[34] Iman Ramezani and Mohammad Bagher Ghofrani. Reconstruction of neutron flux distribution by nodal synthesis method using online in-core neutron detector readings. *Progress in Nuclear Energy*, 131:103574, 2021.

[35] KW Shim, DY Oh, DS Kim, YJ Choi, and YH Park. Colss axial power distribution synthesis using artificial neural network with simulated annealing. *KNS Spring*, pages 24–25, 2015.

[36] Jonathan Tyler Gates. High precision sensing of triga operational characteristics using optical fiber-based gamma thermometers. Master's thesis, Texas AM University, 2022.

[37] Anthony Birri, Tyler Gates, Joshua Jones, and Thomas E. Blue. Data analytic methodology for an optical fiber based gamma thermometer array. In *Transactions of the American Nuclear Society*, volume 123, pages 549–552, Washington, D.C, 2020.

[38] Kathleen Goetz and Sacit Cetiner. Development of a fast-spectrum self-powered neutron detector for use in sodium-cooled fast reactors. In *APS Division of Nuclear Physics Meeting Abstracts*, volume 2019, pages SD–009, 2019.

[39] Kathleen C Goetz, SM Cetiner, and Cihangir Celik. Development of a fast-spectrum self-powered neutron detector for molten salt experiments in the versatile test reactor. In *EPJ Web of Conferences*, volume 253, page 05006. EDP Sciences, 2021.

[40] Farrokh Khoshahval, Minyong Park, Ho Cheol Shin, Peng Zhang, and Deokjung Lee. Vanadium, rhodium, silver and cobalt self-powered neutron detector calculations by rast-k v2.0. *Annals of Nuclear Energy*, 111:644–659, 2018.

[41] David Elliott. *Nuclear power: past, present and future*. IOP Publishing, 2022.

[42] W Robb Stewart and Koroush Shirvan. Construction schedule and cost risk for large and small light water reactors. *Nuclear Engineering and Design*, 407:112305, 2023.

[43] NuScale Power LLC. Nuscale standard plant design certification application, chapter 4, part 2 - tier 2. Technical Report Rev. 5, 2020.

[44] Pavel Suk, Ondřej Chvála, G. Ivan Maldonado, and Jan Frýbort. Simulation of a nuscale core design with the casl vera code. *Nuclear Engineering and Design*, 371:110956, 2021.

[45] Westinghouse Electric Company LLC. AP1000 design control document, chapter 4.3. Technical Report Rev. 19, 2011.

[46] Piotr Darnowski, Patryk Ignaczak, Paweł Obrębski, Michał Stępień, and Grzegorz Niewiński. Simulations of the AP1000-based reactor core with SERPENT computer code. *Archive of Mechanical Engineering*, vol. 65(No 3):295–325, 2018.

[47] Yeshuai Sun, Xing Wang, Changhui Wang, Junhong Lv, Hui Yu, and Yixue Chen. Preliminary analysis of effect of vanadium self-powered neutron detectors on ap1000 reactor core physical parameters. pages 1912–1920, 2017.

[48] Robert Wilcox Candalino. Engineering analysis of low enriched uranium fuel using improved zirconium hydride cross sections. Master's thesis, Texas A&M University, 2006.

[49] Theodore A Parish. Nuclear safety analyses and core design calculations to convert the texas a&m university nuclear science center reactor to low enriched uranium fuel, 1995. DOE/ER/75884-T1.

[50] Ting-Han Lin and Shun-Chi Wu. Sensor fault detection, isolation and reconstruction in nuclear power plants. *Annals of Nuclear Energy*, 126:398–409, 2019.

[51] Ting-Han Lin, Te-Chuan Wang, and Shun-Chi Wu. Deep learning schemes for event identification and signal reconstruction in nuclear power plants with sensor faults. *Annals of Nuclear Energy*, 154:108113, 2021.

[52] Vidya Sagar Yellapu, Weidong Zhang, Vineet Vajpayee, and Xinli Xu. A multiscale data reconciliation approach for sensor fault detection. *Progress in Nuclear Energy*, 135:103707, 2021.

[53] Paolo F Fantoni and Alessandro Mazzola. Multiple-failure signal validation in nuclear power plants using artificial neural networks. *Nuclear Technology*, 113(3):368–374, 1996.